CHEMISTRY OF MATERIALS

Open Access

This article is licensed under CC-BY 4.0

pubs.acs.org/cm

Article

Electron-Enhanced Atomic Layer Deposition of Tunable TiC_xN_y Ternary Nitride Films Using Tetrakis(dimethylamido)titanium with Ammonia Reactive Background Gas

Zachary C. Sobell, Andrew S. Cavanagh, and Steven M. George*

Cite This: *Chem. Mater.* 2026, 38, 4104–4114

Read Online

ACCESS | Metrics & More | Article Recommendations

ABSTRACT: Electron-enhanced atomic layer deposition (EE-ALD) of amorphous, tunable titanium carbonitride (TiC_xN_y) films was obtained at low temperatures. The TiC_xN_y EE-ALD was achieved using sequential exposures of tetrakis(dimethylamido)titanium (TDMAT) and low-energy electrons in the presence of a continuous NH_3 reactive background gas (RBG). The composition of the TiC_xN_y films was tuned by varying the NH_3 background pressure and the electron exposure time. The TiC_xN_y EE-ALD was performed by utilizing a hollow cathode plasma electron source (HC-PES). The HC-PES delivered a high electron flux into background gases at pressures up to several mTorr. TDMAT was used as the source of Ti, C, and N. The NH_3 RBG served as both a source of additional N and a method for the removal of C from the TiC_xN_y films. The TiC_xN_y EE-ALD film growth was monitored using in situ ellipsometry. The TiC_xN_y EE-ALD was conducted at low temperatures that never exceeded 130 °C, using NH_3 pressures from 0 to 3 mTorr. The C content in the TiC_xN_y films could be tuned using the NH_3 RBG pressure. Lower NH_3 pressures led to the incorporation of more C into the TiC_xN_y films. The C:Ti ratio varied from ~0.3 to ~0.05 versus NH_3 RBG pressure, as measured by X-ray photoelectron spectroscopy (XPS), at a constant electron exposure time of 10 s. Electron exposure time was also used to modulate the C content in the TiC_xN_y films. Shorter electron exposures led to more C incorporation. The C:Ti ratio varied from ~2 to ~0.1 versus electron exposure time, as measured by XPS at a constant NH_3 background pressure of 2 mTorr. In situ 4-wavelength and ex situ spectroscopic ellipsometry were able to estimate electrical resistivities for the TiC_xN_y films. Resistivity was reduced from >2000 $\mu\Omega$ cm to ~200 $\mu\Omega$ cm with decreasing C content. X-ray reflectivity (XRR) measurements were able to determine film densities. The film density for TiN films was 4.6 g/cm^3, and the film density decreased with increasing C content. The C content in the TiC_xN_y films could also be varied using a CH_4 RBG. Carbon could be added by carbon EE-chemical vapor deposition (EE-CVD) using electron exposures together with a CH_4 RBG. The carbon could also be removed by carbon EE-chemical vapor etching (EE-CVE) using electron exposures together with NH_3 RBG. The C content in the TiC_xN_y films was difficult to control using a supercycle approach with TiN EE-ALD and carbon EE-CVD.

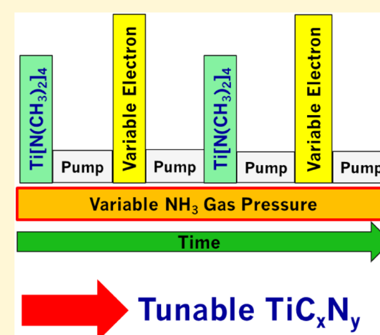

Downloaded via UNIV OF COLORADO BOULDER on April 28, 2026 at 16:33:51 (UTC).
See https://pubs.acs.org/sharingguidelines for options on how to legitimately share published articles.

1. INTRODUCTION

Electron-enhanced atomic layer deposition (EE-ALD) using low energy electrons can deposit semiconductor, metal, and dielectric films. GaN,[1] Si,[2] BN,[3] Co,[4,5] Ru,[6] and SiO_2[7] have all been deposited using EE-ALD. EE-ALD grows these films utilizing alternating exposures of precursors and low energy electrons at ≤100−150 eV. During the EE-ALD process, the precursor adsorbs on the substrate. The subsequent electron exposure is able to remove the ligands from the adsorbed precursor through electron stimulated desorption (ESD).[8] Open sites that are left behind by the desorbed ligands are then available for further precursor adsorption. EE-ALD growth results from repeating the alternating precursor and electron exposures. EE-ALD is a nonthermal process and can deposit materials at low temperatures <100 °C.

A model system for EE-ALD is the deposition of Si from disilane (Si_2H_6).[2] In previous investigations, silicon was deposited using sequential exposures of Si_2H_6 and low energy electrons at room temperature.[2] Si_2H_6 is first dissociatively adsorbed on the surface. Then hydrogen is removed by ESD using low energy electron exposures. The hydrogen ESD leaves behind dangling bonds that are then available for the next Si_2H_6 adsorption. Silicon growth rates were measured to be 0.3 Å/cycle at an electron energy of 100 eV.[2] This silicon growth rate was in agreement with the calculated silicon growth rate determined by dissociative adsorption of Si_2H_6 on the dangling bonds on the Si surface.[2]

Received: December 13, 2025
Revised: March 25, 2026
Accepted: March 30, 2026
Published: April 7, 2026

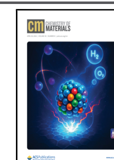

© 2026 The Authors. Published by American Chemical Society

https://doi.org/10.1021/acs.chemmater.5c03380
Chem. Mater. 2026, 38, 4104−4114

EE-ALD can also be conducted in the presence of a reactive background gas (RBG). TiN EE-ALD was performed earlier using tetrakis(dimethylamido)titanium (TDMAT) and electron exposures with a NH_3 background gas as shown in Figure 1.[9] The electrons were derived from a hollow cathode plasma

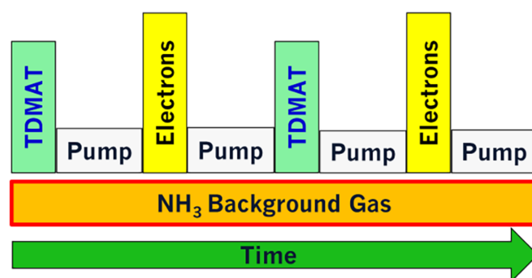

Figure 1. Schematic of TiC_xN_y EE-ALD process with reactive NH_3 background gas (RBG) showing alternating TDMAT precursor and low energy electron exposures separated by pumping. NH_3 RBG is flowed into the reactor during entire EE-ALD cycle.

electron source (HC-PES).[4] Employing a RBG during EE-ALD is feasible because the HC-PES has chemical insensitivity and is tolerant of pressures in the vacuum chamber up to ≤10 mTorr.

Alternating TDMAT and low energy electron exposures deposited a TiC_xN_y film with significant carbon content during TiN EE-ALD.[9] In contrast, the deposition of a highly pure, low-carbon, low-resistivity, crystalline TiN film was possible using long electron exposures and sufficient NH_3 RBG pressure during the entire TiN EE-ALD cycle.[9] The C and O impurities were believed to be removed by the reaction of NH_3 and low energy electrons to create reactive $\bullet NH_2$ and $\bullet H$ radicals and possibly NH_x^+ ions. These species can react with C and O impurities to form volatile CH_3NH_2, NO_x, or H_2O products.

EE-ALD and focused electron beam induced deposition (FEBID) techniques employ similar strategies to obtain high purity materials. During FEBID, a focused electron beam with energies of ∼1 keV in the presence of a chemical precursor can deposit nanostructured features.[10] The purity of FEBID can be affected by postdeposition cleaning with electron beams and reactive gases.[11,12] Background gases during FEBID can also be utilized to obtain higher purity materials.[13,14] In addition, EE-chemical vapor deposition (EE-CVD) can also produce high purity materials using RBGs. A recent survey of EE-CVD demonstrated the growth of high purity silicon and tungsten-containing films such as SiN, SiC_x, W_2N, WO_x and WC_x.[15] These films were obtained using volatile silicon and tungsten precursors concurrent with electron exposures and various RBGs such as NH_3, CH_4 and O_2.[15]

Titanium nitride has a long history of use as a diffusion barrier in back-end-of-the-line microprocessor manufacturing.[16−20] Without a diffusion barrier such as titanium nitride, Cu readily diffuses into Si and SiO_2.[21−23] Titanium carbonitride (TiC_xN_y) films also have utility as diffusion barriers for the same application.[24−27] Moreover, ternary nitrides like TiC_xN_y should have enhanced barrier properties. Compared with pure TiN, the addition of carbon should restrict the crystallinity of TiC_xN_y films and lead to fewer grain boundaries for Cu diffusion. Ultrathin TiC_xN_y diffusion barriers in small vias and trenches are also important to maximize the amount of space that can be occupied by the Cu conducting line.[28,29] Rapid nucleation of TiC_xN_y is critical to produce ultrathin continuous TiC_xN_y films. Long nucleation times will lead to thicker and rougher films prior to obtaining continuous films. TiC_xN_y films also have tunable optical, electronic, and mechanical properties that depend on the film composition.[30,31]

Ternary films have been deposited previously using physical vapor deposition (PVD), chemical vapor deposition (CVD), and ALD techniques.[32−34] PVD methods include sputtering, laser ablation, and electric arc deposition.[33] TiC_xN_y has been deposited by reactive sputtering with an N_2 background gas and a mixed Ti−C target.[26,35] The N content was varied by changing the N_2 flow rate. Other TiC_xN_y sputtering studies have employed a pure Ti target together with N_2 and CH_4 gases.[27] CVD can also be used to deposit ternary nitrides. TiC_xN_y CVD has been performed by the thermal decomposition of TDMAT.[24,25] The TiC_xN_y CVD was conducted using a showerhead gas delivery located over a silicon wafer at 275−395 °C.[24,25] Other TiC_xN_y CVD has been performed using a gas flow of $TiCl_4$−CH_3CN−H_2 at 885 °C.[36]

Deposition of TiN using thermal ALD is difficult because the TiN ALD films have high porosity and C contamination when using TDMAT together with NH_3 as the precursors.[23,37] TiN plasma ALD can be employed to avoid these issues.[23] Likewise, TiC_xN_y films can also be deposited using plasma ALD techniques.[38,39] For the plasma TiC_xN_y ALD, TDMAT was employed together with either H_2, NH_3 or H_2/CH_4.[38,39] TiC_xN_y thermal ALD may also be possible using the supercycle approach.[32,40,41] During the supercycle procedure, one or several cycles of the TiC ALD[42] could be performed together with one or several cycles of the TiN ALD[23] to obtain a tunable composition of the TiC_xN_y film.

This work developed a new approach to deposit TiC_xN_y ternary films using EE-ALD methods. TiC_xN_y EE-ALD films were deposited using sequential TDMAT and electron exposures with a continuous NH_3 RBG. The TiC_xN_y EE-ALD film growth was monitored using in situ ellipsometry. TiC_xN_y films with tunable C content were obtained by varying the NH_3 reactive background gas pressures and the electron exposure times. The composition of the TiC_xN_y EE-ALD films was analyzed using in situ Auger electron spectroscopy (AES) and ex situ X-ray photoelectron spectroscopy (XPS) studies. The resistivity of the TiC_xN_y EE-ALD films was measured using in situ and ex situ ellipsometry.

2. EXPERIMENTAL SECTION

2.1. Vacuum Chamber and Accessories

The vacuum apparatus used to grow the EE-ALD films has been described previously.[1−5,9] A turbomolecular pump was attached to the main vacuum chamber. This turbomolecular pump has a pumping speed of 245 L/s for Ar (HiPace 300 P, Pfeiffer Vacuum Technology AG). The turbomolecular pump was also backed by a smaller turbomolecular pump operating at a pumping speed of 67 L/s for Ar (HiPace 80, Pfeiffer Vacuum Technology AG). This smaller turbomolecular pump was backed by a rotary vane pump (Pascal 2010 SD 10 m^3/h, Pfeiffer Vacuum Technology AG). Additionally, the main vacuum chamber could be pumped by an ion pump (TiTan 100L Variable Element, 100 L/s, Gamma Vacuum). A valve separated this ion pump from the main chamber. Using both the ion and turbomolecular pumps, the main vacuum chamber had a base pressure of 2×10^{-9} Torr.

Samples could be introduced without breaking vacuum using a load lock.[2] The main chamber also contained an in situ ellipsometer (Filmsense FS-1) and mass spectrometer (PrismaPlus QMG 220,

https://doi.org/10.1021/acs.chemmater.5c03380
Chem. Mater. 2026, 38, 4104−4114

Pfeiffer Vacuum). The chamber was also equipped with a cold cathode gauge (MKS) to measure pressure. In addition, a picoammeter (Keithley) was attached to the sample stage to measure the electron current going to ground through the sample and sample stage. The sample temperature was measured with a thermocouple held in contact to the coupon surface with a clip. An analysis chamber that contained an in vacuo Auger electron spectroscopy (AES) spectrometer (RBD, microCMA) was also connected to the main chamber.[2]

2.2. Hollow Cathode Plasma Electron Source

The electron source was a hollow cathode plasma electron source (HC-PES) that has been described in detail earlier.[4] An argon (Airgas, 99.999%) plasma was ignited in the hollow cathode body. A bias grid was used to extract and accelerate the low energy electrons. The electrons exited the HC through an aperture. Argon gas also leaked through this aperture and produced a pressure of ∼1 mTorr in the reactor. All the work in this study used an applied voltage of −100 V to the bias grid.

Electron optics were used to separate the electrons from any sputtered material from the hollow cathode plasma.[4] The electrons also traveled through the argon gas and the RBG on their path to the sample. The distance between the bias grid located close to the aperture and the sample was ∼30 cm.[4] The electrons were incident on the sample at normal incidence. The electron currents measured at the sample were in the range of 31−54 mA.

The electron energy defined by the grid bias was ≤100 eV. The electron beam irradiated an area of ~ 20 cm^2 on the sample stage. During each experiment, the samples started at room temperature at 21 °C. The interaction between the low energy electrons and the substrate led to minor sample heating. The sample temperature never exceeded 130 °C for the experiments with the most cycles and the longest electron exposures.

The electron flux can be estimated from the electron current and the area of the electron beam on the sample stage. The circular area of the sample stage irradiated by the electron current is ~ 20 cm^2. A measured electron current of 50 mA over this area produces an electron flux of ~ 2.5 mA/cm^2. This electron flux is equivalent to $\sim 1.6 \times 10^{16}$ electrons/(cm^2 s). Assuming a density of surface sites of $1 \times 10^{15}/cm^2$, this electron flux produces ∼16 electrons per surface site per second.

The spatial distribution of the electron beam is approximately Gaussian. A larger number of electrons will be incident at the center of the sample stage and fewer electrons will be incident at the edges of the circular sample area irradiated by the electrons. This Gaussian distribution can affect the uniformity of the EE-ALD film. Longer electron beam exposures are required to achieve saturation at the edges of the circular sample area irradiated by the electron beam. The effect of the Gaussian distribution on saturation and film growth during EE-ALD was studied in earlier investigations of Co EE-ALD.[5]

2.3. Reactive Background Gas and Substrates

The NH_3 reactive background gas (RBG) (NH_3, Matheson, 99.9992%) flowed into the chamber using a mass flow controller (MFC, MKS) and was continuously present during the EE-ALD process. The RBG pressure was measured by the cold cathode pressure gauge (MKS) under constant pumping using the turbomolecular pump. The NH_3 flow rates were 0, 0.2, 0.8, 1.7, 5.9, 8, and 13 SCCM. These flow rates corresponded to NH_3 pressures of 0, 0.03, 0.2, 0.8, 1.4, 2, and 3.3 mTorr, respectively. More flow rates were employed near the lower limit of the MFC to determine the TiC_xN_y EE-ALD film growth characteristics in the region of low NH_3 pressure. The flow rate of 0 SCCM was ensured by closing a valve upstream of the MFC to block any NH_3 leakage.

Electron scattering occurs between the electron beam and background gases in the chamber. The RBG pressure typically varied from the high 10^{-4} Torr range to the mid 10^{-3} Torr range. This pressure window allows for electron beam interaction with the RBG without excessive electron scattering. These pressures facilitate the creation of gas-phase radicals and ions that can influence the EE-ALD film composition. The incoming electron beam on the substrate at normal incidence also ensured direct electron-surface interactions.

The EE-ALD was conducted on Si wafer coupons (Silicon Valley Microelectronics, boron-doped) with a sample area of ~ 10 cm^2. There was a native oxide on the silicon surface for all the film growth experiments. Prior to the experiments, the Si native oxide coupons were sonicated in dilute Alconox Detergent, rinsed in DI water, then blown dry with ultrahigh purity nitrogen. The coupons were then loaded into the load lock chamber following previously defined procedures.[4]

2.4. EE-ALD Pulse Sequences

TiC_xN_y EE-ALD was conducted using alternating precursor and electron beam exposures as shown in Figure 1. The pulse sequence was: (1) TDMAT exposure; (2) pumping before electron beam exposure; (3) electron beam exposure; and (4) pumping before the next TDMAT exposure. The timing for this pulsing sequence can be characterized by (t_1, t_2, t_3, t_4). The TDMAT precursor was maintained at 0.3 Torr behind a micropulse valve. The TDMAT bubbler was heated to ∼45 °C to achieve the required vapor pressure. The valve was actuated for $t_1 = 1$ s. The valve opening led to a transient pressure in the main chamber of 4×10^{-7} Torr. This transient pressure was measured by the cold cathode gauge in an empty reactor without the NH_3 RBG.

The TDMAT precursor pressure at the sample was higher than the reported pressure transient. This higher pressure occurs because the micropulse valve used to dose the precursors was connected to a 1/4 inch diameter tube that led to the sample and ended ∼5 cm from the sample. In contrast, the cold cathode gauge measured the precursor pressure transient after the pressure transient had diffused into the entire chamber and was pumped by the turbomolecular pump. The TDMAT precursor adsorption displayed weak self-limiting behavior. Smaller TDMAT precursor exposures were chosen to obtain somewhat lower film growth rates. These lower growth rates ensured that the RBGs can affect the full thickness of the most recently deposited film layer.

The electron exposure was performed with a grid bias of −100 V for $t_3 = 0.5$, 1, 2, 5, 10, or 20 s, with an electron current measured at the sample stage of ∼30−50 mA. The next TDMAT adsorption was then conducted after continued pumping for $t_4 = 1$ s after the electron exposure. The timing for this pulsing sequence was (1, 1, t_3, 1). The sum of these steps produced a reaction cycle time of ∼3.5 to 23 s. Note that the turbomolecular pump was pumping on the main vacuum chamber during the entire pulse sequence.

2.5. Spectroscopic Ellipsometry, X-ray Reflectivity, and X-ray Photoelectron Spectroscopy

In situ ellipsometry measurements were collected every second during the deposition. The in situ ellipsometer (FilmSense FS-1) employed four wavelengths of light. The in situ ellipsometry measurements of film thickness had a precision within ± 0.03 Å. Films were modeled with a Drude−Lorentz model. The longest wavelength used in the FS-1 ellipsometer is 660 nm. This wavelength is not sufficient to accurately model the Drude term. Therefore, the measured in situ resistivities are only estimations.

Ex situ spectroscopic ellipsometry (Model M-2000, J.A. Woollam Co., Inc.) was also used to corroborate the in situ resistivity measurements. A Drude−Lorentz model was also employed to model the ex situ spectroscopic ellipsometry results. The ex situ resistivities were consistently measured to be higher than the in situ resistivities.

X-ray reflectivity (XRR) was used to determine film density. Grazing incidence X-ray diffraction (GI-XRD) determined the crystallinity of the films. Both XRR and GI-XRD scans were performed using an XRD instrument (Bede D1, Jordan Valley Semiconductors) with radiation from Cu Kα ($\lambda = 1.540$ Å). The X-ray tube filament voltage was 40 kV and the current was 35 mA. The incident angle used for the GI-XRD measurements was 0.3°. The XRR scan range was 300 to 6000 arcsec with a 5 arcsec step size. The XRR scans were analyzed using modeling software (REFS, Jordan Valley Semiconductors).

Measurable XRD peaks consistent with crystalline TiN were found for a sample grown with NH_3 pressures at 0.8 mTorr and electron exposures at 10 s. In contrast, minimal to no XRD peaks were found for the TiC_xN_y EE-ALD films grown with lower NH_3 pressures and shorter electron exposures. Some samples may exhibit nanocrystallinity too fine for GI-XRD quantification.

An X-ray photoelectron spectrometer (PHI 5600) using a monochromatic Al Kα source with an energy of 1486.6 eV was used to determine the film composition. The pass energy was 58.7 eV, the step size was 0.25 eV, and the dwell time was 50 ms per step. An electron beam neutralizer was used during the XPS measurements. The Ar ion beam energy during depth profiling was 3 keV. The XPS data were collected using AugerScan (RBD Instruments) software. The XPS data were analyzed employing CASA XPS (Casa Software Ltd.) software. All compositional data from XPS analysis were collected after 90 s of Ar ion sputtering to remove atmospheric oxidation and adventitious C.

3. RESULTS AND DISCUSSION

TiN EE-ALD films were grown earlier using sequential TDMAT and electron exposures with an NH_3 reactive background gas.[9] High purity TiN films with no carbon were produced in the limit of long electron exposures and large NH_3 exposures.[9] In this study, the electron exposures and NH_3 exposures were both varied to obtain a tunable carbon composition in the TiC_xN_y EE-ALD films.

3.1. Variation of Electron Exposure Time

Electron-enhanced deposition of TiC_xN_y films with tunable carbon content were grown by varying the electron exposure time with a fixed NH_3 background pressure of 2 mTorr. Figure 2 displays results for the TiC_xN_y EE-ALD performed with electron exposures of 1 s and a NH_3 pressure of 2 mTorr. The timing sequence with time in seconds was (1, 1, 1, 1). The TiC_xN_y EE-ALD growth per cycle (GPC) was 0.63 Å/cycle. The growth per cycle was constant even though the sample temperature was increasing slowly from room temperature up to 55 °C resulting from electron beam heating during this experiment. The TiC_xN_y EE-ALD film growth was linear at all electron exposure times and displayed rapid nucleation.

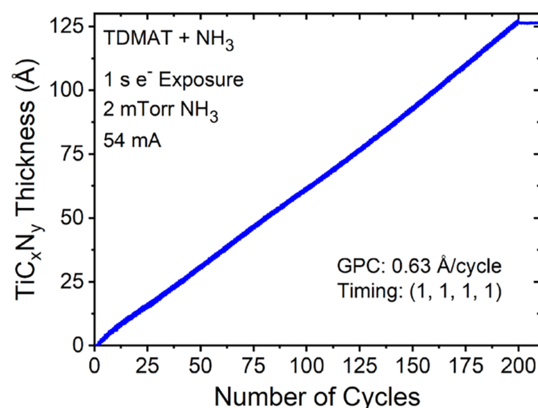

Figure 2. TiC_xN_y film thickness during 200 cycles of TiC_xN_y EE-ALD on Si native oxide measured by in situ ellipsometry. Growth rate of 0.63 Å/cycle was obtained with NH_3 background pressure of 2 mTorr and timing sequence with time in seconds of (1, 1, 1, 1).

Figure 3 shows an expansion of the TiC_xN_y film thickness versus number of EE-ALD cycles for the first 10 cycles in Figure 2. The TiC_xN_y film nucleates rapidly and nearly linear growth of 0.63 Å/cycle is observed after the second cycle. The changes in the TiC_xN_y film thickness are very digital with the TDMAT and electron exposures. The TiC_xN_y thickness increases during the TDMAT exposure and then decreases during the electron exposures. Because the TDMAT exposures displayed weak self-limiting behavior, the TiC_xN_y thickness in Figure 3 increased until the TDMAT exposure was stopped after the 1 s TDMAT exposure.

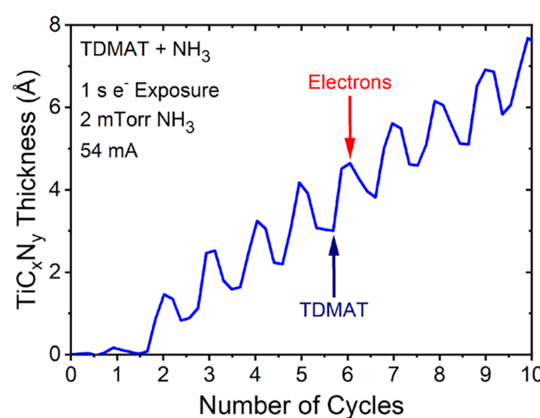

Figure 3. Initial growth during first 10 cycles of TiC_xN_y EE-ALD in Figure 2 showing rapid nucleation of TiC_xN_y film growth. In situ ellipsometry measurements can monitor the digital nature of film growth resulting from sequential TDMAT and electron exposures.

The optical model for the TiC_xN_y film observes the addition and subtraction of the surface species. The adsorption of TDMAT on the sample introduces highly polarizable methyl groups to the surface.[43,44] The ellipsometry model accounts for this increase in polarizability as an increase in sample thickness. The removal of the methyl groups by the combination of electron flux and active NH_x and H radical and ion species from the NH_3 RBG leads to a corresponding decrease in this surface component of the model film thickness.

TiC_xN_y EE-ALD films were grown using a variety of electron exposure times with the timing sequence of (1, 1, x, 1). The TiC_xN_y EE-ALD growth rates were relatively constant over the various reaction conditions. Ex situ XPS was used to measure the carbon in the TiC_xN_y films. Figure 4 shows the C:Ti ratio in the TiC_xN_y films versus the electron exposure time. The C:Ti ratio was chosen as a metric because some of the films oxidized when exposed to air. In Figure 4, films grown with shorter electron exposures of 0.5, 1, and 2 s displayed

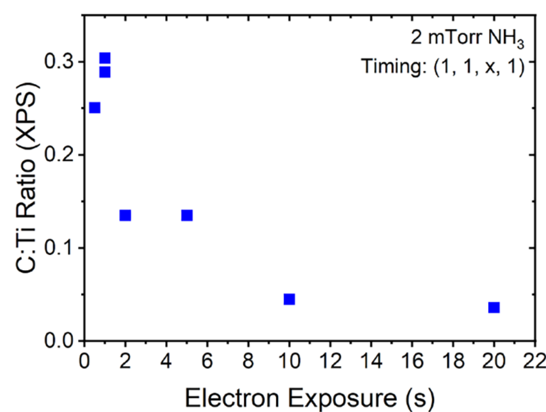

Figure 4. Ex situ XPS of C:Ti ratio in TiC_xN_y films grown with varying electron exposures with a NH_3 background pressure of 2 mTorr and timing sequence of (1, 1, x, 1).

https://doi.org/10.1021/acs.chemmater.5c03380
Chem. Mater. 2026, 38, 4104−4114

measurable ex situ oxidation. In vacuo AES could not be used to quantify the N content in the TiC_xN_y films. The primary N AES peak overlaps with the primary Ti AES peak.[9] Unfortunately, there were no other useable N AES peaks.

The C:Ti ratio should stay constant during atmospheric oxidation if the TiC_xN_y oxidation is preferential to the TiN component of the film. In support of this assumption, TiC has been shown to be more oxidation resistant than TiN.[45] Additionally, the N content decreases with increasing oxygen content as measured by ex situ XPS. This trend is most pronounced for the TiC_xN_y EE-ALD films grown with electron exposures of 0.5, 1, and 2 s that had the most oxidation.

The TiC_xN_y film density measured by XRR versus electron exposure time is shown in Figure 5. Film density increases with longer electron exposure times. These results, together with the results in Figure 4, indicate that longer electron exposure times result in lower C content and higher density TiC_xN_y films. The maximum measured TiC_xN_y density after an electron exposure for 20 s is 4.6 g/cm^3. This density for the lowest carbon composition of $TiC_{0.04}N_{1.28}$ can be compared to the bulk density of TiN at 5.4 g/cm^3, TiC at 4.9 g/cm^3, and Ti at 4.5 g/cm^3.

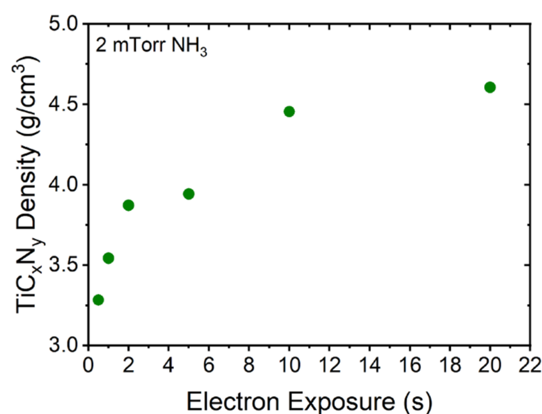

Figure 5. Ex situ X-ray reflectivity (XRR) measurements of the density of TiC_xN_y films grown with varying electron exposures and a NH_3 background pressure of 2 mTorr.

Previous TiN EE-ALD studies reported a density of 5.3 g/cm^3 after long electron exposures for a film with a composition of $TiC_{0.03}N_{1.17}$.[9] The lower density observed in the current work may result from the increased N content in the film. The decrease in density with superstoichiometric TiN was reported previously.[46] Excess N in TiN has been documented previously as well.[9,19] In comparison, films grown with shorter electron exposures of 0.5 and 1 s displayed significantly lower densities. This low density may enable larger ex situ oxidation due to high porosity.

The TiC_xN_y EE-ALD growth rates were fairly constant versus electron exposure time. The growth rates were 0.56, 0.63, 0.65, 0.64, 0.57, and 0.46 Å/cycle for electron exposure times of 0.5, 1, 2, 5, 10, and 20 s, respectively. The growth rates peak at electron exposure times around 2 s. The growth rates then decrease slightly with increasing electron exposures up to 20 s.

Short electron exposure times may not be long enough to create many active sites on the sample surface to allow for more precursor adsorption. As electron exposures increase in length, the available adsorption site density should increase. However, the growth rate then decreases slightly at longer electron exposure times. There may be competitive electron-enhanced etching that occurs at longer electron exposure times. Additionally, the film density increases and C content decreases at longer electron exposure times. These changes could both reduce the TiC_xN_y growth per cycle.

Ellipsometry was also able to estimate the electrical resistivity of the films. In situ 4-wavelength and ex situ spectroscopic ellipsometry were used to measure the film resistivity. Figure 6 shows that the film resistivity decreases

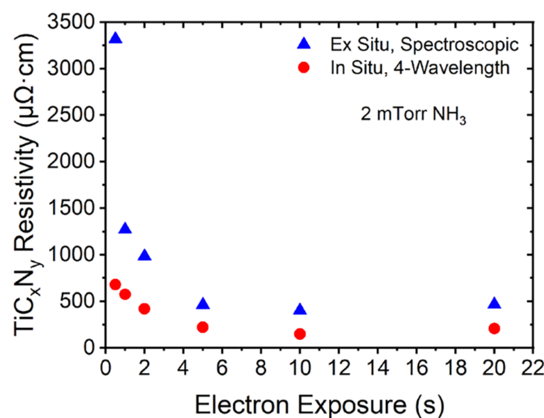

Figure 6. In situ and ex situ spectroscopic ellipsometry estimations of the resistivity of TiCN films grown with varying electron exposures and a NH_3 background pressure of 2 mTorr.

with increasing electron exposure time and the corresponding lower C content in the TiC_xN_y EE-ALD films. The lowest electrical resistivity of 208 $\mu\Omega$ cm is obtained after an electron exposure for 20 s. This measured resistivity is comparable with the resistivity of 120 $\mu\Omega$ cm measured earlier for TiN EE-ALD films.[9]

The TiC_xN_y electrical resistivity increases progressively for electron exposures ≤10 s when carbon concentration increases for these shorter electron exposures. The in situ resistivity increases dramatically from 419 to 575 to 679 $\mu\Omega$ cm for electron exposures of 2, 1, and 0.5 s when the film composition changes from $TiC_{0.13}N_{1.22}$ to $TiC_{0.30}N_{1.10}$ and then $TiC_{0.25}N_{1.04}$, respectively. In addition, there is a much higher ex situ resistivity compared with in situ resistivity for the films grown with 0.5 s electron exposures. This behavior suggests that the TiC_xN_y EE-ALD films with high C content have high porosity and facile oxidation in air.

The increase in the electrical resistivity of TiC_xN_y with increasing carbon content has been observed in previous investigations. The electrical resistivity for sputtered TiC_xN_y films was 80−90 $\mu\Omega$ cm for film compositions between 10 and 40 mol % carbon.[46] The resistivity then increased dramatically to ∼250 $\mu\Omega$ cm at ∼50 mol % carbon and then to 600 $\mu\Omega$ cm at ∼70 mol % carbon.[46] An even higher electrical resistivity of ∼3000 $\mu\Omega$ cm was measured for $Ti_{0.38}N_{0.34}C_{0.27}O_{0.01}$ films grown by CVD with TDMAT.[25] Measurements of the optical resistivity of sputtered TiC_xN_y films also increased progressively from 15 mol % carbon to 60 mol % carbon.[31]

3.2. Variation of NH_3 Pressure

The C content of TiC_xN_y EE-ALD films could also be tuned by varying the NH_3 RBG pressure with a fixed electron exposure time of 10 s. Figure 7 shows the growth of a TiC_xN_y EE-ALD film with a low NH_3 RBG pressure of 0.03 mTorr and

https://doi.org/10.1021/acs.chemmater.5c03380
Chem. Mater. 2026, 38, 4104−4114

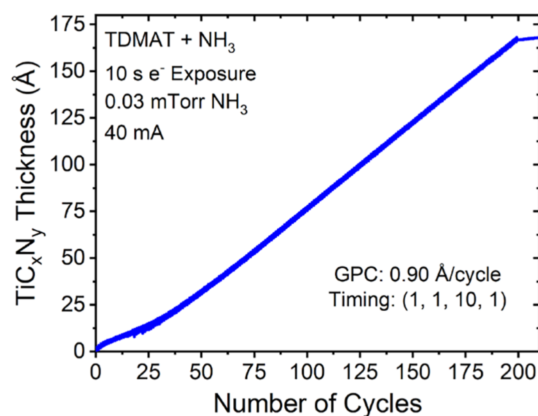

Figure 7. TiC_xN_y film thickness during 200 cycles of TiC_xN_y EE-ALD on Si native oxide measured by in situ ellipsometry. Growth rate of 0.90 Å/cycle was obtained with NH_3 background pressure of 0.03 mTorr and timing sequence of (1, 1, 10, 1).

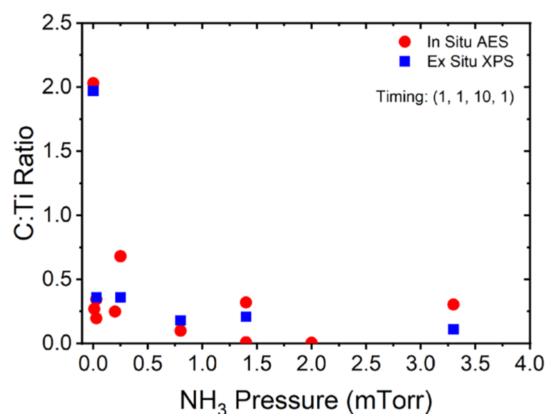

Figure 8. In situ AES and ex situ XPS measurements of C:Ti ratio of TiC_xN_y films grown with varying NH_3 background pressures and timing sequence of (1, 1, 10, 1).

an electron exposure time of 10 s with a timing sequence of (1, 1, 10, 1). The TiC_xN_y EE-ALD film growth is linear with a GPC of 0.90 Å/cycle. There is also a rapid nucleation on the Si coupon with native oxide. TiC_xN_y EE-ALD films grown at other NH_3 RBG pressures with the same timing sequence of (1, 1, 10, 1) also displayed linear growth and rapid nucleation.

The TiC_xN_y EE-ALD growth rates were dependent on the NH_3 RBG pressure. Growth rates were 0.37, 0.90, 0.88, 0.93, 0.79, and 0.57 Å/cycle for 0, 0.03, 0.2, 0.8, 1.4, and 3.3 mTorr, respectively. The growth rate was low for the two extrema in NH_3 RBG pressure at 0 and 3.3 mTorr. The absence of NH_3 RBG provides no activation of the surface through interaction with NH_x and H radicals and ions. This lack of activation may produce a low uptake of TDMAT on subsequent exposures and a low overall growth rate.

The NH_3 RBG leads to interaction between the low energy electrons and NH_3 and the production of active NH_x and H species. These active species allow for the creation of more TDMAT adsorption sites and yield larger growth rates. The growth rate is relatively constant at NH_3 pressures of 0.03, 0.2, 0.8 mTorr with values of 0.90, 0.88, and 0.93 Å/cycle, respectively. At higher NH_3 pressures of 1.4 and 3.3 mTorr, there is more C removal from the films. The increasing film density contributes to the lower measured growth rates of 0.79 and 0.57 Å/cycle, respectively. At these higher NH_3 RBG pressures, there also may be competitive etching that accounts for some decrease in the growth rate.

Figure 8 displays the C:Ti ratio from the in situ AES measurements and the ex situ XPS analysis versus NH_3 pressure. The C:Ti ratio of 2.0 is much higher for no NH_3 pressure with an electron exposure of 10 s compared with the C:Ti ratio of 0.25−0.3 for 0.5 and 1 s electron exposures with an NH_3 pressure of 2 mTorr in Figure 4. This behavior suggests that the NH_3 RBG is effective at removing carbon even with short electron exposures or low NH_3 pressures.

Figure 8 also shows that there is a rapid drop in the C:Ti ratio at low increasing NH_3 pressures. Then the C:Ti ratio slowly decreases for larger NH_3 pressures. The larger NH_3 RBG pressures result in more interaction between the low energy electrons and the NH_3 RBG. These interactions create more NH_x and H active species. These active species remove more C from the TiC_xN_y EE-ALD film and decrease the C:Ti ratio.

The TiC_xN_y EE-ALD film density was also measured versus the NH_3 RBG pressure with an electron exposure time of 10 s. The TiC_xN_y film densities are shown in Figure 9. The density

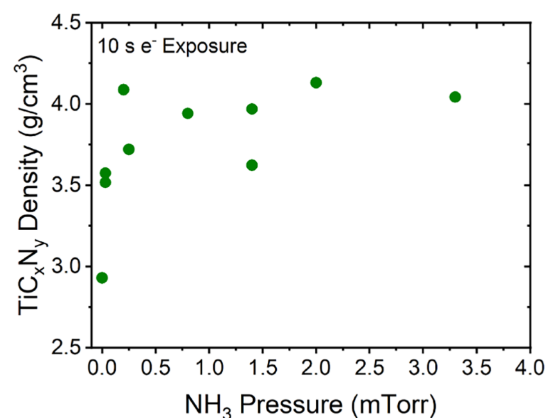

Figure 9. Ex situ XRR measurements of density of TiC_xN_y films grown with varying NH_3 background pressures and electron exposures of 10 s.

increases rapidly between no NH_3 and NH_3 RBG pressures of 0.25 mTorr. Similar to the ability of NH_3 RBG pressure to decrease the C:Ti ratio shown in Figure 8, small NH_3 RBG pressures are able to increase the TiC_xN_y film density. Lower C content in the TiC_xN_y films is again correlated with higher density TiC_xN_y films. The TiC_xN_y density of ∼4.0 g/cm^3 obtained with electron exposures of 10 s is slightly less than the highest TiC_xN_y density of ∼4.6 g/cm^3 observed in Figure 5 with electron exposures of 20 s. This comparison suggests that longer electron exposures lead to higher film densities.

Resistivities were also measured for the TiC_xN_y EE-ALD films using in situ and ex situ ellipsometry versus NH_3 RBG pressure. The resistivity results are shown in Figure 10. Higher C content in the films corresponds to higher measured resistivities. The magnitude of these electrical resistivities are similar to the electrical resistivities in Figure 6. The films grown with no NH_3 have high C content and the highest resistivities.

The ex situ ellipsometry measurements are consistently higher than the in situ ellipsometry measurements. These differences are again attributed to some oxidation of the TiC_xN_y EE-ALD films upon air exposure. The ex situ resistivity

https://doi.org/10.1021/acs.chemmater.5c03380
Chem. Mater. 2026, 38, 4104−4114

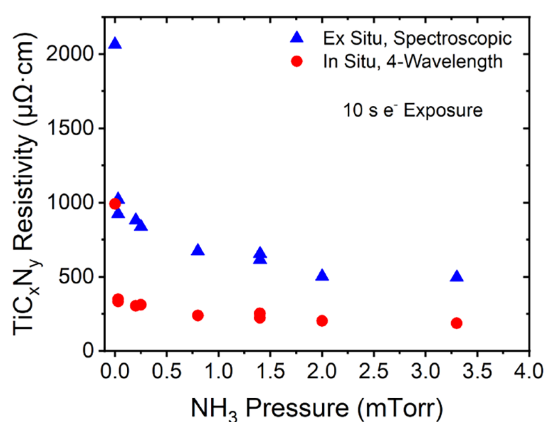

Figure 10. In situ and ex situ spectroscopic ellipsometry estimations of resistivity of TiC_xN_y films grown with varying NH_3 partial pressures and electron exposure of 10 s.

of 2100 $\mu\Omega$ cm with no NH_3 and a 10 s electron exposure time in Figure 10 is less than the ex situ resistivity of 3300 $\mu\Omega$ cm with a NH_3 RBG pressure of 2 mTorr with 0.5 s electron exposure in Figure 6. This suggests more oxidation resistance for the TiC_xN_y films grown with longer electron exposures. The TiC_xN_y film density was also higher for TiC_xN_y films grown with longer electron exposures.

3.3. Mechanism for Tunable C in TiC_xN_y Films

The TDMAT precursor contains Ti, C, and N. Figure 4 shows that the TiC_xN_y EE-ALD films have a C:Ti ratio of 0.25−0.30 with NH_3 RBG pressures of 2 mTorr for short electron exposures of 0.5 or 1 s. The C:Ti ratio then is reduced progressively versus electron exposure time. Figure 8 also shows that the C:Ti ratio is ∼2.0 with no NH_3 RBG for electron exposures of 10 s. The C:Ti ratio is then reduced by higher NH_3 RBG pressures with the 10 s electron exposure time. The ability of longer electron exposure times and higher NH_3 RBG pressures to reduce the C content of the TiC_xN_y EE-ALD is attributed to the interaction between low energy electrons with the NH_3 RBG and the growing TiC_xN_y film. These interactions are illustrated in Figure 11.

During the electron exposure, the interaction between the electrons and the NH_3 RBG will lead to dissociation and dissociative ionization.[47] Figure 11 shows the electrons dissociating NH_3 to produce $\bullet NH_2$ and $\bullet H$ radical species. These reactive species could then abstract R, the dimethylamino ligand, from the surface. In addition, the electrons could remove the dimethylamino ligand by the process of electron stimulated desorption (ESD).[48,49] The electrons could also fragment the dimethylamino ligand and leave carbon behind on the surface. The removal of dimethylamino ligands by either ESD or abstraction and fragmentation of the dimethylamino ligand to deposit carbon on the surface is shown in step (A) of Figure 11.

Electron dissociation to produce $\bullet NH_2$ and $\bullet H$ radical species can also lead to the adsorption of these radical species on the surface. In addition, NH_3 may be able to adsorb directly on the reactive sites. Possible Ti−H species that may form during this process could be converted to Ti-NH_2 species by the high $\bullet NH_2$ flux. The formation of Ti-NH_2 surface species by adsorption of $\bullet NH_2$ or NH_3 is shown in step (B) of Figure 11.

Carbon could also be removed from the surface by the $\bullet NH_2$ flux during longer electron exposures (not shown). Shorter electron exposures or lower NH_3 RBG pressures may not yield sufficient $\bullet NH_2$ flux for this C cleaning process. Abstraction of C by $\bullet H$ radicals is not believed to be a major pathway for C removal as suggested by the low etch rate of C films in the presence of H_2 RBG and electron flux that is discussed in Section 3.4.

Subsequently, hydrogen ESD could remove the H from Ti-NH_2 species to produce reactive dangling bond sites on the surface. These reactive sites would be on N surface species. This process is illustrated in step (C) of Figure 11. During the TDMAT exposure, the TDMAT precursor could then adsorb on the reactive dangling bond sites on the surface. This adsorption would form new Ti−N bonds on the N active sites. The TDMAT adsorption on dangling bond sites is illustrated in step (D) of Figure 11. Based on this proposed mechanism, the C content in the TiC_xN_y EE-ALD films could be tuned by using shorter electron exposures or lower NH_3 RBG pressures that do not lead to the removal of C from the dimethylamino ligands on the surface.

The relative influence on TiC_xN_y EE-ALD from electron interactions with either the gas phase or surface species is still

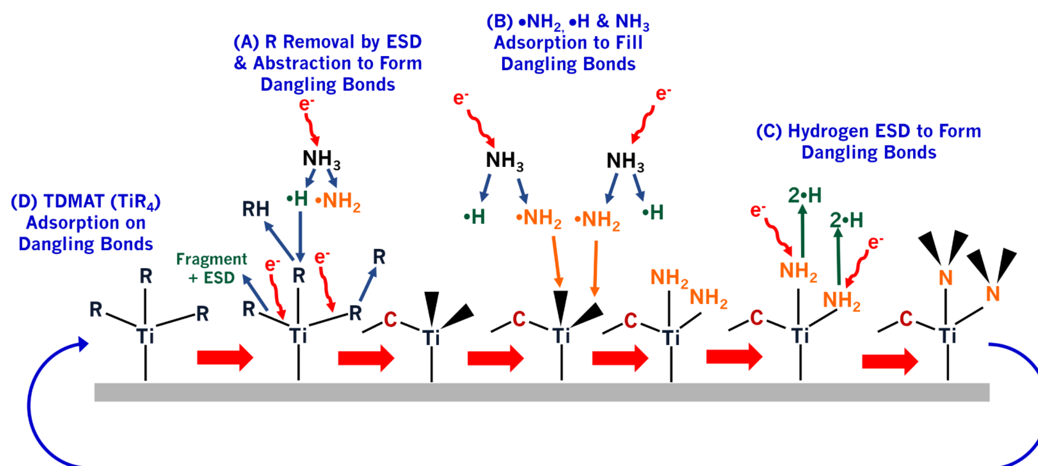

Figure 11. TiC_xN_y growth mechanism involving (A) alkyl group removal by ESD and abstraction by NH_2 and H radicals to form dangling bonds; (B) NH_2, H and NH_3 adsorption to fill dangling bonds; (C) hydrogen ESD to form dangling bonds; and (D) TDMAT adsorption on dangling bonds.

https://doi.org/10.1021/acs.chemmater.5c03380
Chem. Mater. 2026, 38, 4104−4114

an open question. As illustrated in Figure 11, •NH_2 and •H radical species reactions with the surface after electron-induced dissociation of NH_3 could affect TiC_xN_y EE-ALD. ESD by electrons incident on the surface could also influence TiC_xN_y EE-ALD. The background gas pressures in the chamber during TiC_xN_y EE-ALD are in the low mTorr range. Electron beam attenuation is not observed until pressures in the high mTorr range. This observation is consistent with minimal electron beam scattering by the background gas under the experimental conditions. However, the relative importance of electron interactions with gas phase and surface species is not known at this time.

3.4. Adding Carbon to TiN Using CH_4 RBG and Carbon Etching Using NH_3 RBG

Carbon can be incorporated in the TiC_xN_y films by varying the electron exposure or the NH_3 background pressure. This C content in these TiC_xN_y films is from the TDMAT organometallic precursor. In addition, C can be incorporated by using a carbon-containing RBG. This study explored the use of a CH_4 RBG to incorporate exogenous carbon in the TiC_xN_y film. These investigations determined that carbon EE-chemical vapor deposition (EE-CVD) films can be deposited using electron exposures together with a CH_4 RBG. Other previously developed methods to deposit carbon films include physical vapor deposition (PVD), chemical vapor deposition (CVD), and thermal conversion techniques.[50,51]

EE-CVD methods are similar to recently developed electron CVD (e-CVD) techniques.[52,53] During EE-CVD, an electron beam with energies of ≤100−150 eV is incident on the substrate in the presence of precursor molecules and other possible background gases.[15] During e-CVD, low energy plasma electrons with energies of 0.3−5 eV are accelerated to a positively biased substrate in the presence of metal precursor molecules.[54] These electrons are believed to reduce the metal center in various metal precursor molecules to deposit metallic films.[52,53]

Figure 12 shows the growth of a carbon EE-CVD film using only electron exposures together with a CH_4 RBG at a pressure of 4 mTorr. The C EE-CVD film growth in Figure 12 is linear versus time with a growth rate of 41 Å/min. Other studies determined that the growth rates for C EE-CVD films were dependent on CH_4 pressures in the reactor. Consequently, the rate of C incorporation into the TiC_xN_y films could be controlled directly by the CH_4 pressure.

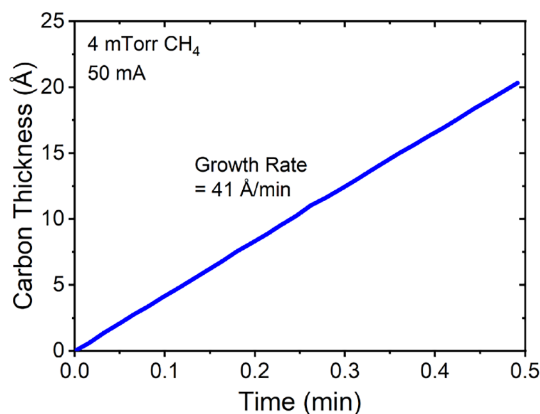

Figure 12. Carbon thickness versus time during C EE-CVD at a CH_4 pressure of 4 mTorr with an electron current of 50 mA. Carbon growth rate was 41 Å/min.

C EE-CVD is proposed to be deposited by the interaction of CH_4 with the low energy electrons. This interaction leads to the creation of CH_x radicals and ions. These species can then adsorb on the substrate. Further irradiation of the CH_x surface species leads to H electron stimulated desorption. The removal of H allows for the adsorption of more CH_x radicals and ions on the surface. This proposed mechanism for C EE-CVD has similarities to the mechanism for diamond CVD.[55]

The exogenous carbon could be added to the TiC_xN_y EE-ALD films using a supercycle approach. A TiN EE-ALD film could be grown in the first part of the supercycle. Carbon could then be added by C EE-CVD with CH_4 RBG in the second part of the supercycle. Carbon could also be added during TiC_xN_y EE-ALD using both CH_4 and NH_3 RBGs together with the electron exposures. Carbon should add if the C deposition rate is higher than the C removal rate in the presence of the NH_3 RBG. The removal of C from the TiC_xN_y films can occur because the NH_3 RBG together with electron exposures can eliminate carbon as shown in Figure 4.

C EE-CVD films can also be etched using NH_3 RBG together with electron exposure. Figure 13 shows the loss of carbon thickness from a C EE-CVD film versus time using a NH_3 RBG pressure of 2 mTorr. The reduction of the C EE-CVD film thickness is linear versus time with an etch rate of 6 Å/min. These results support the interpretation that the NH_3 RBG is able to remove C from TiC_xN_y films during TiC_xN_y EE-ALD. As discussed earlier, the interaction of low energy electrons and the NH_3 RBG leads to the production of NH_x and H radicals and ions. These active species can react with C in the TiC_xN_y films and form volatile etch products. These products may take the form of simple C−N compounds like CH_3NH_2 (methylamine).

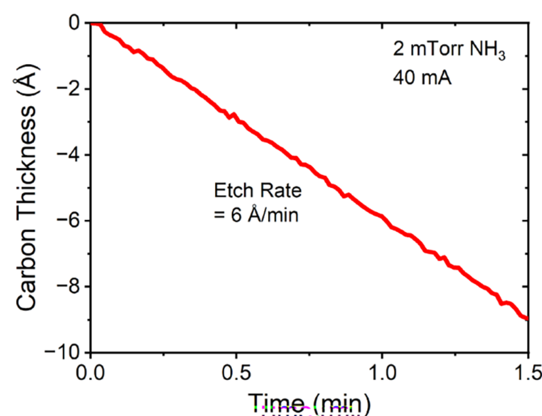

Figure 13. Carbon thickness versus time during C EE-CVE at a NH_3 pressure of 4 mTorr with an electron current of 50 mA. Carbon etch rate was 6 Å/min.

Additional studies explored the ability of O_2 and H_2 RBGs to etch the C EE-CVD films. The largest etch rates of 30 Å/min were observed with O_2 RBG at a pressure of 0.5 mTorr. The smallest etch rates of <1 Å/min were measured with H_2 RBG at a pressure of 2 mTorr. The larger etch rate of 6 Å/min for NH_3 RBG at a pressure of 2 mTorr compared with the etch rate of <1 Å/min for H_2 RBG at a pressure of 2 mTorr suggests that C removal during TiC_xN_y EE-ALD results primarily from the •NH_2 radical species.

https://doi.org/10.1021/acs.chemmater.5c03380
Chem. Mater. 2026, 38, 4104−4114

Although C EE-CVD could be employed to add C to TiC_xN_y films, controlling the C content proved to be difficult using the supercycle approach with TiN EE-ALD and C EE-CVD. The C EE-CVD is rapid and tuning the C content required variable low CH_4 RBG pressures and shorter electron exposures. Greater regulation over the low CH_4 RBG pressure would be necessary to obtain similar control of the C content as demonstrated in Figure 4 for variable electron exposures and Figure 8 for different NH_3 pressures.

4. CONCLUSIONS

TiC_xN_y EE-ALD was performed using sequential exposures of TDMAT and low energy electrons with a continuous NH_3 reactive background gas (RBG). The TiN EE-ALD was conducted utilizing a HC-PES that can deliver a high electron flux into background gases at pressures up to several mTorr. TiN EE-ALD films were grown at temperatures that did not exceed 130 °C using electron energies of ≤100 eV. Electron exposures were varied from 0.5 to 20 s and NH_3 pressures were varied from 0 to ~3.3 mTorr. Shorter electron exposures and lower NH_3 RBG pressures allowed for the incorporation of C into the films.

Sequential TDMAT and low energy electron exposures with no NH_3 RBG led to the deposition of a porous C-rich film that underwent facile atmospheric oxidation. The introduction of NH_3 RBG greatly increased the density and removed C from the films. The interaction between NH_3 and the low energy electrons is believed to create active species in the form of NH_x and H radicals and ions that affect film composition. Longer electron exposures and higher NH_3 RBG pressures increased the production of these active species and led to more C removal and increased the film density.

As the electron exposures were increased from 0.5 to 20 s, the C:Ti ratio fell from ~0.3 to ~0.03 as measured by ex situ XPS. This ~10× reduction in C occurred at a fixed NH_3 pressure of 2 mTorr. The density and resistivity of these TiC_xN_y films also increased and decreased, respectively, with increasing electron exposure times. Films grown with a longer electron exposure were less susceptible to ex situ oxidation.

As NH_3 pressures were increased from 0 to 3 mTorr, the C:Ti ratio fell from ~2 to ~0.1 as measured by ex situ XPS. This 20x reduction in C occurred at a fixed electron exposure of 10 s. The density and resistivity of these films also increased and decreased, respectively, with increasing NH_3 pressure. Films with less C and higher densities were less susceptible to ex situ oxidation.

Attempts were made to control the C content in the TiC_xN_y films by adding C using a CH_4 RBG. Carbon EE-CVD films could be grown using a CH_4 RBG with electron exposure. These carbon EE-CVD films could also be etched using NH_3 RBG with electron exposures. Unfortunately, the C content in TiC_xN_y films was hard to control using a supercycle approach involving TiN EE-ALD and carbon EE-CVD.

■ AUTHOR INFORMATION

Corresponding Author

Steven M. George − *Department of Chemistry, University of Colorado Boulder, Boulder, Colorado 80309-0215, United States*; orcid.org/0000-0003-0253-9184; Email: Steven.George@Colorado.edu

Authors

Zachary C. Sobell − *Department of Chemistry, University of Colorado Boulder, Boulder, Colorado 80309-0215, United States*

Andrew S. Cavanagh − *Department of Chemistry, University of Colorado Boulder, Boulder, Colorado 80309-0215, United States*; orcid.org/0000-0002-6201-530X

Complete contact information is available at: https://pubs.acs.org/10.1021/acs.chemmater.5c03380

Notes

The authors declare no competing financial interest.

■ ACKNOWLEDGMENTS

This work was supported by the Center for Heterogeneous Integration of Microelectronic Systems (CHIMES), one of the seven centers sponsored by the Semiconductor Research Corporation (SRC) and DARPA under the Joint University Microelectronics Program 2.0 (JUMP 2.0). The authors thank Rebecca Hirsch for the GIXRD and XRR measurements. The authors also acknowledge Kenneth Smith and Don David from the University of Colorado Integrated Instrument Development Facility for their construction and maintenance of the HC-PES and computer interfacing.

■ REFERENCES

(1) Sprenger, J. K.; Cavanagh, A. S.; Sun, H.; Wahl, K. J.; Roshko, A.; George, S. M. Electron Enhanced Growth of Crystalline Gallium Nitride Thin Films at Room Temperature and 100°C Using Sequential Surface Reactions. *Chem. Mater.* **2016**, *28*, 5282−5294.

(2) Sprenger, J. K.; Sun, H.; Cavanagh, A. S.; George, S. M. Electron-Enhanced Atomic Layer Deposition of Silicon Thin Films at Room Temperature. *J. Vac. Sci. Technol., A* **2017**, *36* (1), 01A118.

(3) Sprenger, J. K.; Sun, H.; Cavanagh, A. S.; Roshko, A.; Blanchard, P. T.; George, S. M. Electron-Enhanced Atomic Layer Deposition of Boron Nitride Thin Films at Room Temperature and 100°C. *J. Phys. Chem. C* **2018**, *122*, 9455−9464.

(4) Sobell, Z. C.; Cavanagh, A. S.; Boris, D. R.; Walton, S. G.; George, S. M. Hollow Cathode Plasma Electron Source for Low Temperature Deposition of Cobalt Films by Electron-Enhanced Atomic Layer Deposition. *J. Vac. Sci. Technol., A* **2021**, *39*, 042403.

(5) Sobell, Z. C.; Cavanagh, A. S.; George, S. M. Growth of Cobalt Films at Room Temperature Using Sequential Exposures of Cobalt Tricarbonyl Nitrosyl and Low Energy Electrons. *J. Vac. Sci. Technol., A* **2019**, *37*, 060906.

(6) Collings, M. A.; Junige, M.; Cavanagh, A. S.; Wang, V.; Kummel, A. C.; George, S. M. Electron-Enhanced Atomic Layer Deposition of Ru Thin Films Using $Ru(DMBD)(CO)_3$ and Effect of Forming Gas Anneal. *J. Vac. Sci. Technol., A* **2023**, *41*, 062408.

(7) Gertsch, J. C.; Sobell, Z. C.; Cavanagh, A. S.; Simka, H.; George, S. M. Electron-Enhanced SiO_2 Atomic Layer Deposition at 35 °C Using Disilane and Ozone or Water as Reactants. *J. Vac. Sci. Technol., A* **2023**, *41*, 042404.

(8) Ramsier, R. D.; Yates, J. T. Electron-Stimulated Desorption: Principles and Applications. *Surf. Sci. Rep.* **1991**, *12*, 243−378.

(9) Sobell, Z. C.; George, S. M. Electron-Enhanced Atomic Layer Deposition of Titanium Nitride Films Using an Ammonia Reactive Background Gas. *Chem. Mater.* **2022**, *34*, 9624−9633.

(10) Utke, I.; Hoffmann, P.; Melngailis, J. Gas-Assisted Focused Electron Beam and Ion Beam Processing and Fabrication. *J. Vac. Sci. Technol. B* **2008**, *26*, 1197−1276.

(11) Rohdenburg, M.; Boeckers, H.; Brewer, C. R.; McElwee-White, L.; Swiderek, P. Efficient NH_3-Based Process to Remove Chlorine from Electron Beam Deposited Ruthenium Produced from $(\eta^3$-$C_3H_5)Ru(CO)_3Cl$. *Sci. Rep.* **2020**, *10*, 1−13.

(12) Spencer, J. A.; Barclay, M.; Gallagher, M. J.; Winkler, R.; Unlu, I.; Wu, Y. C.; Plank, H.; McElwee-White, L.; Fairbrother, D. H. Comparing Postdeposition Reactions of Electrons and Radicals with Pt Nanostructures Created by Focused Electron Beam Induced Deposition. *Beilstein J. Nanotechnol.* **2017**, *8*, 2410−2424.

(13) Perentes, A.; Hoffmann, P. Focused Electron Beam Induced Deposition of Si-based Materials from SiO_xC_y to Stoichiometric SiO_2: Chemical Compositions, Chemical-Etch Rates, and Deep Ultraviolet Optical Transmissions. *Chem. Vap. Deposition* **2007**, *13*, 176−184.

(14) Shawrav, M. M.; Taus, P.; Wanzenboeck, H. D.; Schinnerl, M.; Stöger-Pollach, M.; Schwarz, S.; Steiger-Thirsfeld, A.; Bertagnolli, E. Highly Conductive and Pure Gold Nanostructures Grown by Electron Beam Induced Deposition. *Sci. Rep.* **2016**, *6*, 34003.

(15) Sobell, Z. C.; Cavanagh, A. S.; George, S. M. Electron-Enhanced Deposition of Titanium-, Silicon- and Tungsten-Containing Films at Low Temperatures Using Volatile Precursors with Various Reactive Background Gases. *Chem. Mater.* **2025**, *37*, 4652−4664.

(16) Paranjpe, A.; IslamRaja, M. Chemical Vapor Deposition TiN Process for Contact/Via Barrier Applications. *J. Vac. Sci. Technol. B* **1995**, *13*, 2105−2114.

(17) Rha, S. K.; Lee, W. J.; Lee, S. Y.; Hwang, Y. S.; Lee, Y. J.; Kim, D. I.; Kim, D. W.; Chun, S. S.; Park, C. O. Improved TiN Film as a Diffusion Barrier Between Copper and Silicon. *Thin Solid Films* **1998**, *320*, 134−140.

(18) Uhm, J.; Jeon, H. TiN Diffusion Barrier Grown by Atomic Layer Deposition Method for Cu Metallization. *Jpn. J. Appl. Phys., Part 1* **2001**, *40* (40), 4657−4660.

(19) Wang, S. Q.; Raaijmakers, I.; Burrow, B. J.; Suthar, S.; Redkar, S.; Kim, K. B. Reactively Sputtered TiN as a Diffusion Barrier between Cu and Si. *J. Appl. Phys.* **1990**, *68*, 5176−5187.

(20) Kaloyeros, A. E.; Eisenbraun, E. Ultrathin Diffusion Barriers/Liners for Gigascale Copper Metallization. *Annu. Rev. Mater. Sci.* **2000**, *30*, 363−385.

(21) Weber, E. R. Transition Metals in Silicon. *Appl. Phys. A.* **1983**, *30*, 1−22.

(22) McBrayer, J. D.; Swanson, R. M.; Sigmon, T. W. Diffusion of Metals in Silicon Dioxide. *J. Electrochem. Soc.* **1986**, *133*, 1242−1246.

(23) Musschoot, J.; Xie, Q.; Deduytsche, D.; Van den Berghe, S.; Van Meirhaeghe, R. L.; Detavernier, C. Atomic Layer Deposition of Titanium Nitride from TDMAT Precursor. *Microelectron. Eng.* **2009**, *86*, 72−77.

(24) Eizenberg, M.; Littau, K.; Ghanayem, S.; Liao, M.; Mosely, R.; Sinha, A. K. Chemical Vapor Deposited TiCN: A New Barrier Metallization for Submicron Via and Contact Applications. *J. Vac. Sci. Technol., A* **1995**, *13*, 590−595.

(25) Eizenberg, M.; Littau, K.; Ghanayem, S.; Mak, A.; Maeda, Y.; Chang, M.; Sinha, A. K. TiCN - A New Chemical-Vapor-Deposited Contact Barrier Metallization for Submicron Devices. *Appl. Phys. Lett.* **1994**, *65*, 2416−2418.

(26) Wenzel, R.; Goesmann, F.; Schmid-Fetzer, R. Diffusion Barriers in Gold-Metallized Titanium-Based Contact Structures on SiC. *J. Mater. Sci. - Mater. Electron.* **1998**, *9*, 109−113.

(27) Sienna, L. F.; Achete, C. A.; Hirsch, T.; Mattos, O. Characterisation of PVD TiCN Layers By Physical and Electrochemical Methods. *Surf. Eng.* **2005**, *21*, 144−150.

(28) Gall, D. Electron Mean Free Path in Elemental Metals. *J. Appl. Phys.* **2016**, *119*, 085101.

(29) Gall, D. The Search for the Most Conductive Metal for Narrow Interconnect Lines. *J. Appl. Phys.* **2020**, *127*, 050901.

(30) Forn, A.; Picas, J. A.; Fuentes, G. G.; Elizalde, E. Mechanical and Tribological Properties of TiC_xN_{1-X} Wear Resistant Coatings. *Int. J. Refract. Met. Hard Mater.* **2001**, *19*, 507−513.

(31) Fuentes, G. G.; Elizalde, E.; Sanz, J. M. Optical and Electronic Properties of TiC_xN_y Films. *J. Appl. Phys.* **2001**, *90*, 2737−2743.

(32) Mackus, A. J. M.; Schneider, J. R.; MacIsaac, C.; Baker, J. G.; Bent, S. F. Synthesis of Doped, Ternary, and Quaternary Materials by Atomic Layer Deposition: A Review. *Chem. Mater.* **2019**, *31*, 1142−1183.

(33) Tareen, A. K.; Priyanga, G. S.; Behara, S.; Thomas, T.; Yang, M. Mixed Ternary Transition Metal Nitrides: A Comprehensive Review of Synthesis, Electronic Structure, and Properties of Engineering Relevance. *Prog. Solid State Chem.* **2019**, *53*, 1−26.

(34) Greenaway, A. L.; Melamed, C. L.; Tellekamp, M. B.; Woods-Robinson, R.; Toberer, E. S.; Neilson, J. R.; Tamboli, A. C. Ternary Nitride Materials: Fundamentals and Emerging Device Applications. *Annu. Rev. Mater. Res.* **2021**, *51*, 591−618.

(35) Chen, R.; Tu, J. P.; Liu, D. G.; Mai, Y. J.; Gu, C. D. M. Mechanical and Tribological Properties of TiCN Nanocomposite Films Deposited by DC Magnetron Sputtering. *Surf. Coat. Technol.* **2011**, *205*, 5228−5234.

(36) Kainz, C.; Tkadletz, M.; Maier-Kiener, V.; Völker, B.; Burtscher, M.; Waldl, H.; Schiester, M.; Thurner, J.; Czettl, C.; Schalk, N. Chemical Vapor Deposited TiCN/TiC Multilayer Coatings: On the Interplay Between Coating Architecture and Mechanical Properties. *Int. J. Refract. Met. Hard Mater.* **2024**, *125*, 106890.

(37) Elam, J. W.; Schuisky, M.; Ferguson, J. D.; George, S. M. Surface Chemistry and Film Growth during TiN Atomic Layer Deposition Using TDMAT and NH_3. *Thin Solid Films* **2003**, *436*, 145−156.

(38) Cho, G.; Rhee, S. -W. Plasma Enhanced Atomic Layer Deposition of TiC_xN_y Film with Various Reactive Gases. *ECS J. Solid State Sci. Technol.* **2014**, 3 (6), P185.

(39) Jeon, S.; Park, S. Tunable Work-Function Engineering of TiC-TiN Compound by Atomic Layer Deposition for Metal Gate Applications. *J. Electrochem. Soc.* **2010**, *157*, H930−H933.

(40) Mahuli, N.; Cavanagh, A. S.; George, S. M. Atomic Layer Deposition of Aluminum Oxyfluoride Thin Films with Tunable Stoichiometry. *J. Vac. Sci. Technol., A* **2020**, *38*, 022407.

(41) Mahuli, N.; Cavanagh, A. S.; George, S. M. Atomic Layer Deposition of Hafnium and Zirconium Oxyfluoride Thin Films. *J. Vac. Sci. Technol., A* **2021**, *39*, 022403.

(42) Hong, T. E.; Choi, S. K.; Kim, S. H.; Cheon, T. Growth of Highly Conformal TiC_x Films Using Atomic Layer Deposition Technique. *J. Am. Ceram. Soc.* **2013**, *96*, 1060−1062.

(43) Burns, K. H.; Srivastava, P.; Elles, C. G. Absolute Cross Sections of Liquids from Broadband Stimulated Raman Scattering with Femtosecond and Picosecond Pulses. *Anal. Chem.* **2020**, *92*, 10686−10692.

(44) Colles, M. J.; Griffith, J. E. Relative and Absolute Raman Scattering Cross Sections in Liquids. *J. Chem. Phys.* **1972**, *56* (7), 3384−3391.

(45) Ajikumar, P. K.; Kamruddin, M.; Ravindran, T. R.; Kalavathi, S.; Tyagi, A. K. Oxidation Behavior of TiC_xN_{1-x} Coatings as a Function of C/N Ratio. *Ceram. Int.* **2014**, *40*, 10523−10529.

(46) Sundgren, J. E.; Johansson, B. O.; Karlsson, S. E.; Hentzell, H. T. G. Mechanisms of Reactive Sputtering of Titanium Nitride and Titanium Carbide II: Morphology and Structure. *Thin Solid Films* **1983**, *105*, 367−384.

(47) Rao, M.; Srivastava, S. K. Total and Partial Ionization Cross-Sections of NH_3 by Electron-Impact. *J. Phys. B: At. Mol. Opt. Phys.* **1992**, *25*, 2175−2187.

(48) Sala, L.; Szymanska, I. B.; Dablemont, C.; Lafosse, A.; Amiaud, L. Response Under Low-Energy Electron Irradiation of a Thin Film of a Potential Copper Precursor for Focused Electron Beam Induced Deposition (FEBID). *Beilstein J. Nanotechnol.* **2018**, *9*, 57−65.

(49) Spencer, J. A.; Rosenberg, S. G.; Barclay, M.; Wu, Y. C.; McElwee-White, L.; Fairbrother, D. H. Understanding the Electron-Stimulated Surface Reactions of Organometallic Complexes to Enable Design of Precursors for Electron Beam-Induced Deposition. *Appl. Phys. A.* **2014**, *117* (4), 1631−1644.

(50) Kim, I.- S.; Shim, C. -E.; Kim, S. -W.; Lee, C. -S.; Kwon, J.; Byun, K. -E.; Jeong, U. Amorphous Carbon Films for Electronic Applications. *Adv. Mater.* **2023**, *35* (43), 2204912.

(51) Zou, J. W.; Reichelt, K.; Schmidt, K.; Dischler, B. The Deposition and Study of Hard Carbon-Films. *J. Appl. Phys.* **1989**, *65*, 3914−3918.

(52) Nadhom, H.; Lundin, D.; Rouf, P.; Pedersen, H. Chemical Vapor Deposition of Metallic Films Using Plasma Electrons as Reducing Agents. *J. Vac. Sci. Technol., A* **2020**, *38*, 033402.
(53) Niiranen, P.; Nadhom, H.; Zanáska, M.; Boyd, R.; Sortica, M.; Primetzhofer, D.; Lundin, D.; Pedersen, H. Biased Quartz Crystal Microbalance Method for Studies of Chemical Vapor Deposition Surface Chemistry Induced by Plasma Electrons. *Rev. Sci. Instrum.* **2023**, *94*, 023902.
(54) Niiranen, P.; Kapran, A.; Nadhom, H.; Cada, M.; Hubicka, Z.; Pedersen, H.; Lundin, D. Plasma Electron Characterization in Electron Chemical Vapor Deposition. *J. Vac. Sci. Technol., A* **2024**, *42*, 023006.
(55) Butler, J. E.; Mankelevich, Y. A.; Cheesman, A.; Ma, J.; Ashfold, M. N. R. Understanding the Chemical Vapor Deposition of Diamond: Recent Progress. *J. Phys.: Condens. Matter.* **2009**, *21*, 364201.

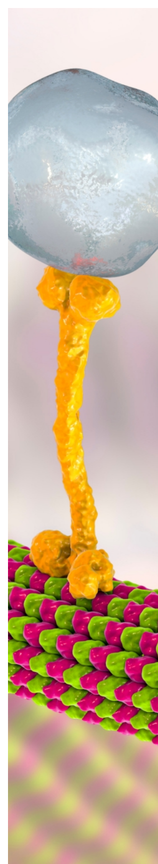
CAS BIOFINDER DISCOVERY PLATFORM™
BRIDGE BIOLOGY AND CHEMISTRY FOR FASTER ANSWERS
Analyze target relationships, compound effects, and disease pathways
Explore the platform

https://doi.org/10.1021/acs.chemmater.5c03380
Chem. Mater. 2026, 38, 4104−4114